Engineering Fracture Mechanics 162 (2016) 290–308

Contents lists available at ScienceDirect

Engineering Fracture Mechanics

journal homepage: www.elsevier.com/locate/engfracmech

Modeling fatigue failure using the variational multiscale method

Shardul Panwar, Shang Sun, Veera Sundararaghavan *

Department of Aerospace Engineering, University of Michigan, Ann Arbor, MI 48105, USA

ARTICLE INFO

Article history:
Received 27 January 2016
Received in revised form 26 May 2016
Accepted 31 May 2016
Available online 2 June 2016

Keywords:
Variational Multi-Scale Method
Fatigue
Cohesive zone model
Crack propagation

ABSTRACT

In this paper, we study fatigue failure using the variational multiscale method (VMM). In the VMM, displacement jumps are represented using finite elements with specially constructed discontinuous shape functions. These elements are progressively added along the crack path during fatigue failure. The stiffness of these elements changes non-linearly in response to the accumulation of damage during cyclic loading. The evolution law for stiffness is represented as a function of traction and the number of loading cycles since the initial onset of failure. Numerical examples illustrate the use of this new methodology for modeling macroscopic crack growth under Mode I loading as well as microscopic crack growth under mixed mode loading within the elastic regime. We find that the discontinuous elements can consistently predict the Mode I stress intensity factor (SIF) and the microstructurally short crack growth paths, and that the computed Paris law for steady crack growth is controlled primarily by two parameters in the decohesion law.

1. Introduction

Numerically, solving a boundary value problem with a crack or multiple cracks inside the domain is not a trivial task, because, these new boundaries (or surfaces) are originally not part of a domain and emerge only as the domain boundaries are loaded. In the context of the finite element method (FEM), the framework of the Galerkin based traditional FEMs are not particularly suited to solve this type of problem. This is due to limitations such as spurious mesh-related length scales [1,2] and the requirement that the mesh be aligned relative to the strain localization band [3,4], which has kinematics similar to that of the crack boundaries. In recent years, however, a whole new class of finite element methods have emerged that can solve the problem of new boundaries emerging inside a domain without experiencing any of the limitations of traditional FEMs. Depending upon how these new boundaries are embedded in the finite element framework, these methods are broadly classified into two families, node enrichment FEM (e.g. X-FEM) and elemental enrichment FEM (e.g. E-FEM). Between these two families, Oliver et al. [5] showed that, under similar conditions, X-FEM is more computationally expensive. Therefore, E-FEM would be a favorable option for problems requiring more computational time. One such problem is fatigue failure, in which crack growth can occur over millions of cycles, so computational solutions are very expensive (in terms of computing time).

* Corresponding author.
E-mail address: veeras@umich.edu (V. Sundararaghavan).
URL: http://umich.edu/~veeras (V. Sundararaghavan).

http://dx.doi.org/10.1016/j.engfracmech.2016.05.021
0013-7944/

Nomenclature

α, β	cohesive fatigue parameters
$\bar{\boldsymbol{r}}, \boldsymbol{r}'$	coarse-scale and fine-scale residual
$\bar{\boldsymbol{u}}, \bar{\boldsymbol{w}}$	continuous coarse-scale displacement fields
$\boldsymbol{\Gamma}^{\boldsymbol{c}}$	crack surface
$[\![\boldsymbol{u}]\!]$	discontinuous displacement field
$\boldsymbol{\sigma}, \boldsymbol{\varepsilon}$	stress, strain
$\boldsymbol{f}$	body force
$\boldsymbol{G}, \boldsymbol{H}$	cracked element out-normal and crack face normal direction
$\boldsymbol{N}, \boldsymbol{B}, \boldsymbol{d}$	standard finite element shape function, shape function gradient, and displacement field nodal values
$\boldsymbol{n}, \boldsymbol{m}$	normal and tangential directions
$\boldsymbol{T}$	external traction
$\boldsymbol{u}', \boldsymbol{w}'$	discontinuous fine-scale displacement fields
$\boldsymbol{u}, \boldsymbol{w}$	displacement field and variation of displacement field
Δ, R	applied displacement and load ratio
$\mathbb{C}, \mathcal{H}_n, \mathcal{H}_m$	material elastic stiffness, Mode-I cohesive stiffness, and Mode-II cohesive stiffness
Ω	domain
J	j-integral
K_I, K_{Ic}	Mode-I stress intensity factor and Mode-I critical stress intensity factor
m, C	Paris curve constants
N_f	number of loading cycles experienced by material point since the onset of failure
T_c^{gb}	critical grain boundary fracture stress
T_{crss}	critical resolved shear stress
W, C_{ij}	strain energy density and HCP material elastic constants

In this paper, we use a type of E-FEM introduced by Hughes [6] and referred to as the variational multiscale method (VMM) by Garikipati [7]. VMM uses a multiscale interpolation scheme to embed cracks into the continuum domain (representing discontinuities using a Heaviside function). The main advantage of the multiscale interpolation scheme over the partition of unity interpolation scheme (used in X-FEM) is the local-to-element nature of the discontinuous displacement field. This means that the additional degree of freedom needed to represent the discontinuity will be condensed out at the element level, thereby leaving the sparsity pattern of the global problem untouched. This is why the computational cost of multiscale interpolation based VMM (E-FEM) is less than the partition of unity interpolation based X-FEM and why the former is more suitable for fatigue problems.

Modeling any crack growth problem requires a correct physical representation of the mechanics of the crack tip. Classically, this is done using Linear Elastic Fracture Mechanics (LEFM), which is based on Griffith's [8] energy-based and Irwin's [9] stress-intensity-factor based theories of crack propagation. Elasticity theory produces stress singularity at the crack tip. In real materials, however, the stresses in front of the crack tip are nonlinear and have finite values. To address this problem, Dugdale [10] and Barenblatt [11] independently developed Cohesive Zone Model (CZM) theory. Willis [12] showed that the CZM is equivalent to Griffith's [8] energy balance concept when the size of the cohesive zone is small compared to the size of the crack and the specimen geometry. Later, Hillerborg et al. [13] introduced the concept of the CZM within the framework of the finite element method. Around the same time, Bažant and Oh [14] introduced the crack band model, which localizes the process zone in a single element. However, this model in the framework of finite element analysis often exhibits mesh orientation bias, meaning that the orientation of the crack band depends on the orientation of the mesh discretization [15]. The CZM, however, regards the fracture process as a gradual separation between the material surfaces, and this separation is resisted by the cohesive tractions. It also defines the stress at the crack tip using a progressive material degradation law. This law, called the Traction–Separation law, specifies a relationship between the crack surface traction and the crack surface separation. For monotonic fracture problems, Xu and Needleman [16] developed a simple form of the CZM to incorporate reversible behavior. In this model, the interfaces heal when brought back into contact after separation. Camacho and Ortiz [17] developed a model in which the unloading and reloading process is reversible. However, during this unloading and reloading event, there is no energy dissipation; thus, this model is not suitable for cyclic loading. De-Andres et al. [18] extended this linear loading and unloading cohesive model to analyze fatigue crack growth in a aluminum shaft. In this model, the damage parameter is adjusted explicitly as the number of loading cycles increases, without any dependence on the damage process occurring within a loading cycle. This results in the lack of predictability of the fatigue crack growth model. Nguyen et al. [19] developed a one-parameter cohesive model that takes into account the irreversible behavior of failure process and the loading–unloading hysteresis. Inspired by this and similar cohesive models [20,21], Maiti and Geubelle [22] developed a two-parameter cohesive model that takes into account all the nonlinear effects associated with failure mechanisms. In their model, once a crack forms, the interface begins to accumulate irreversible damage during the loading part of each cycle,

which reduces the stiffness of the interface. During unloading, the model response is linear, but with a lower slope compared to the previous loading cycle. Maiti and Geubelle [22] used this cohesive model in the framework of the standard finite element method and referred to it as the cohesive/volumetric finite element method (CVFE). However, the use of zero-volume elements or interface elements in the standard finite element framework makes the method subject to the numerical discretization scheme. To solve this issue, we combine the cohesive model developed by Maiti and Geubelle [22] with the VMM. The coupling of a cohesive zone model with the VMM has been demonstrated by Rudraraju et al. [23]. They used a simple linear CZM inside the framework of the VMM to successfully demonstrate crack propagation in laminated fiber reinforced composites and showed experimental comparisons. However, the VMM has not yet been utilized in problems involving cyclic loading. In this paper, we employ a cyclic cohesive zone model, referred to as the fatigue CZM, proposed by Maiti and Geubelle [22] along with the variational multiscale method to predict the steady state crack growth rate in two-dimension.

Using cohesive theory to accurately predict any failure process requires proper calibration of the cohesive model parameters. One approach is to fit the cohesive parameters to one or more experiment(s) and then use those fitted parameters to predict other experimental results. Using this approach, uniaxial tensile tests can be used to determine the cohesive parameters for Mode I fracture [24]. Another approach is to determine these parameters from a lower-scale calculation [25,26]. In case of fatigue failure, Maiti and Geubelle [22] followed the first approach and fitted cohesive parameters to the macro-scale Paris law.

Thus, the objectives of this paper are: (1) to successfully demonstrate the coupling of the fatigue cohesive model with the variational multiscale method, (2) to correctly predict the macro-scale Mode I stress intensity factor, (3) to correlate the experimental micro-structurally short crack path with the VMM crack path, (4) to introduce an approach for calibrating the fatigue cohesive law parameters from the macro experiments, and (5) to show that different steady-state crack growth rates (or Paris laws) can be simulated by different cohesive parameters that control the loading stiffness of the fatigue CZM.

The present paper is divided into three sections. Section 2 gives a brief description of the variational multiscale method. Section 3 describes the cohesive model used for modeling fatigue failure. In Section 4, we present our numerical results for fatigue failure using different representative two-dimensional problems.

2. The Variational Multi-Scale Method (VMM)

The presence of cracks in a continuum domain necessitates a discontinuous representation of the displacement field. A numerical treatment of such discontinuities and the resultant singular strain field was done in the work of Temam and Strang [27], which was on the space BD(Ω) (of functions of bounded deformation). This idea was later used to develop a numerical framework for the problem of strong discontinuities due to strain localization by Simo et al. [28], Simo and Oliver [29], and Armero and Garikipati [1]. Later, this approach was adopted by Garikipati [7] to embed micro-mechanical surface laws into a macroscopic continuum formulation in a multiscale setting. The mathematical model of this variational multiscale method is briefly described in Section 2.1.

2.1. A mathematical model of the variational multiscale method

The crack surface (Γ_c) in a continuous domain (Ω) is shown in Fig. 1. The standard weak form of the balance of linear momentum over the domain (Ω) is given by

$$\int_{\Omega} \nabla^s \boldsymbol{w} : \boldsymbol{\sigma}\, dV = \int_{\Omega} \boldsymbol{w} \cdot \boldsymbol{f}\, dV + \int_{\partial\Omega_t} \boldsymbol{w} \cdot \boldsymbol{T}\, dS \tag{2.1}$$

where $\boldsymbol{\sigma}$ is the stress, $\boldsymbol{w}$ is an admissible displacement variation, $\nabla^s \boldsymbol{w}$ is the symmetric gradient of the variation, $\boldsymbol{T}$ is the external traction and $\boldsymbol{f}$ is the body force. The displacement fields ($\boldsymbol{u}$ and variation $\boldsymbol{w}$) can be decomposed into continuous coarse-scale ($\bar{\boldsymbol{u}}, \bar{\boldsymbol{w}}$) and discontinuous fine-scale ($\boldsymbol{u}', \boldsymbol{w}'$) components. Such a decomposition is possible because of the requirement that the fine-scale fields $\boldsymbol{u}'$ and $\boldsymbol{w}'$ must vanish outside the fine-scale subdomain Ω'. In crack propagation problems, the fine-scale field ($\boldsymbol{u}'$) represents the discontinuity.

$$\boldsymbol{u} = \bar{\boldsymbol{u}} + \boldsymbol{u}' \tag{2.2}$$

$$\boldsymbol{w} = \bar{\boldsymbol{w}} + \boldsymbol{w}' \tag{2.3}$$

$$\bar{\boldsymbol{u}} \in \bar{\boldsymbol{S}} = \{\boldsymbol{v} | \boldsymbol{v} = \boldsymbol{g}\ \boldsymbol{on}\ \partial\boldsymbol{\Omega}_{\boldsymbol{u}}\}$$

$$\bar{\boldsymbol{w}} \in \bar{\boldsymbol{v}} = \{\boldsymbol{v} | \boldsymbol{v} = \boldsymbol{0}\ \boldsymbol{on}\ \partial\boldsymbol{\Omega}_{\boldsymbol{u}}\}$$

$$\boldsymbol{u}' \in \boldsymbol{S}' = \{\boldsymbol{v} | \boldsymbol{v} = \boldsymbol{0}\ \boldsymbol{on}\ \boldsymbol{\Omega} \setminus \boldsymbol{int}(\boldsymbol{\Omega}')\}$$

$$\boldsymbol{w}' \in \boldsymbol{v}' = \{\boldsymbol{v} | \boldsymbol{v} = \boldsymbol{0}\ \boldsymbol{on}\ \boldsymbol{\Omega} \setminus \boldsymbol{int}(\boldsymbol{\Omega}')\}$$

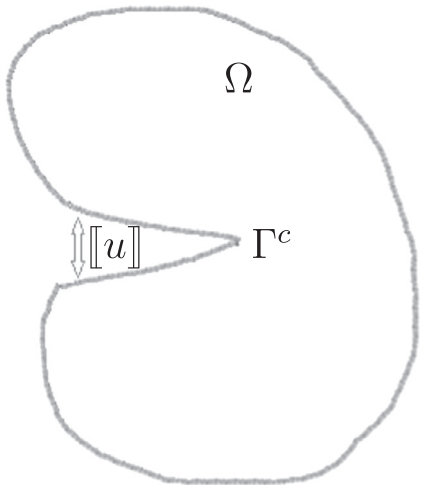

Fig. 1. 2-Dimensional representation of a crack opening $[\![u]\!]$ and the crack surface Γ^c.

where $\boldsymbol{S} \subset \boldsymbol{BD}(\boldsymbol{\Omega}), \boldsymbol{v} \subset \boldsymbol{H}^{\mathbf{1}}(\boldsymbol{\Omega})$, $\boldsymbol{S} = \bar{\boldsymbol{S}} \oplus \boldsymbol{S}'$, and $\boldsymbol{v} = \bar{\boldsymbol{v}} \oplus \boldsymbol{v}'$. $\bar{\boldsymbol{v}}$ and $\boldsymbol{v}'$ are chosen to be linearly independent. More concisely, the choice of space $\bar{\boldsymbol{S}}$ at the elemental level can be represented using linear polynomials, while space $\boldsymbol{S}'$ contains non-nodal supported functions (e.g. discontinuities) that are independent from $\bar{\boldsymbol{S}}$.

Using this additive decomposition, the weak form (2.1) can be separated into two equations, one involving only the coarse-scale variation $\bar{\boldsymbol{w}}$, and another involving only the fine-scale variation $\boldsymbol{w}'$.

$$\int_{\Omega} \nabla^{\boldsymbol{s}} \bar{\boldsymbol{w}} : \boldsymbol{\sigma}\, dV = \int_{\Omega} \bar{\boldsymbol{w}} \cdot \boldsymbol{f}\, dV + \int_{\Gamma_h} \bar{\boldsymbol{w}} \cdot \boldsymbol{T}\, dS \tag{2.4}$$

$$\int_{\Omega} \nabla^{\boldsymbol{s}} \boldsymbol{w}' : \boldsymbol{\sigma}\, dV = \int_{\Omega} \boldsymbol{w}' \cdot \boldsymbol{f}\, dV + \int_{\Gamma_h} \boldsymbol{w}' \cdot \boldsymbol{T}\, \boldsymbol{dS} \tag{2.5}$$

Eq. (2.5) can be simplified by using integration by parts and variational arguments to [7]:

$$\int_{\Gamma^c} \boldsymbol{w}' \boldsymbol{\sigma} \cdot \boldsymbol{n}\, dS = \int_{\Gamma^c} \boldsymbol{w}' \cdot \boldsymbol{T}^{\boldsymbol{c}}\, dS \tag{2.6}$$

where $\boldsymbol{T}^{\boldsymbol{c}}$ is the external traction on the crack faces.

2.2. The micro-mechanical surface law

The micro-mechanics of crack growth (Fig. 2) can be explained by a traction–separation law. This traction–separation law is inserted into the continuum formulation through Eq. (2.6). The traction $\boldsymbol{T}^{\boldsymbol{c}}$ is decomposed into two components (for 2-D problems), one normal to the crack face (T_n^c) and another tangent to the crack face (T_m^c).

$$\boldsymbol{T}^{\boldsymbol{c}} = T_n^c \boldsymbol{n} + T_m^c \boldsymbol{m} \tag{2.7}$$

The fine scale-field $\boldsymbol{u}'$, which is composed of a displacement discontinuity $[\![\boldsymbol{u}]\!]$, can be similarly decomposed into its components $[\![u_n]\!]$ (opening) and $[\![u_m]\!]$ (shear) along the $\boldsymbol{n}$ and $\boldsymbol{m}$ directions respectively.

$$[\![\boldsymbol{u}]\!] = [\![u_n]\!]\boldsymbol{n} + [\![u_m]\!]\boldsymbol{m} \tag{2.8}$$

Using the above two Eqs. (2.7) and (2.8), the micro-mechanical cohesive law (discussed in Section 4) can be utilized by specifying the relationship between traction components and discontinuous displacement components in both the normal and tangential directions. For the case of monotonic loading, a simple surface traction law is used, given by [30]:

$$T_n^c = T_{n0}^c - \mathcal{H}_n [\![u_n]\!], \quad T_m^c = T_{m0}^c - \mathcal{H}_m [\![u_m]\!] \tag{2.9}$$

where T_{n0}^c and $\mathcal{H}_n$ are the Mode I critical opening traction and Mode I softening modulus, respectively, and T_{m0}^c and $\mathcal{H}_m$ are the Mode II critical opening traction and Mode II softening modulus, respectively. In Section 3, we modify the surface traction law to account for cyclic irreversibility.

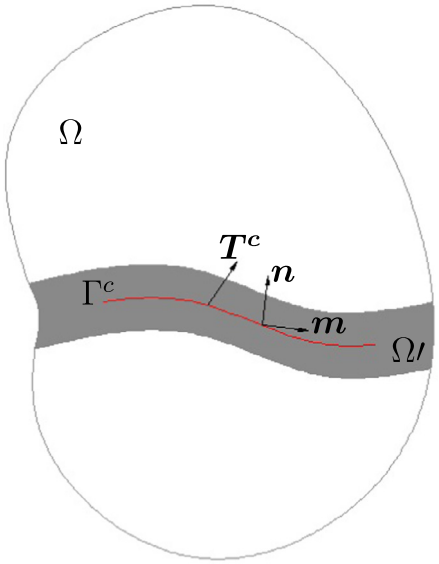

Fig. 2. Micro-structural domain Ω' and crack surface Γ^c, along with crack directions normal $\boldsymbol{n}$ and tangent $\boldsymbol{m}$.

2.3. Finite-dimensional formulation (2-dimensional)

In a finite-dimensional setting, the domain Ω can be divided into a number of connected non-overlapping elements such that $\Omega = \cup_1^{\boldsymbol{nel}} \Omega_e^h$, where ***nel*** represents the number of elements in the finite domain. The fine-scale displacement $\boldsymbol{u}'$ can be written in terms of local interpolation functions as:

$$\boldsymbol{u}'_{\boldsymbol{e}} = \boldsymbol{M}_{\boldsymbol{T}^c} [\![\boldsymbol{u}]\!]_{\boldsymbol{e}} \tag{2.10}$$

where $[\![\boldsymbol{u}]\!]_{\boldsymbol{e}}$ is the elemental value of the fine-scale displacement discontinuity. $\boldsymbol{M}_{\boldsymbol{T}^c}$ is a multiscale shape function given by

$$\boldsymbol{M}_{\boldsymbol{T}^c} = \boldsymbol{N} - \boldsymbol{H}_{\boldsymbol{T}^c} \tag{2.11}$$

where $\boldsymbol{N}$ is the usual linear shape function for triangular elements, and $\boldsymbol{H}_{\boldsymbol{T}^c}$ is the Heaviside function, which is used to introduce a discontinuity within the sub domain Γ_c. This construction ensures that $\boldsymbol{M}_{\boldsymbol{T}^c} = \boldsymbol{0}$ on $\Omega \setminus int(\Omega')$. The construction of this multiscale shape function $\boldsymbol{M}_{\boldsymbol{T}^c}$ in two-dimensions is shown in Fig. 3. In the weak form, $\boldsymbol{M}_{\boldsymbol{T}^c}$ comes into the system of equation as $\nabla \boldsymbol{M}_{\boldsymbol{T}^c}$ through the expression for $\nabla \boldsymbol{u}'$.

$$\nabla \boldsymbol{u}' = \nabla \boldsymbol{M}_{\boldsymbol{T}^c} [\![\boldsymbol{u}]\!] \tag{2.12}$$

where

$$[\![\boldsymbol{u}]\!] = \begin{bmatrix} [\![u]\!]_x \\ [\![u]\!]_y \end{bmatrix}, \quad \nabla \boldsymbol{M}_{\boldsymbol{T}^c} = \frac{1}{h^i} \boldsymbol{G} - \delta_{\Gamma^c} \boldsymbol{H},$$

$$\boldsymbol{G} = \begin{bmatrix} n_x^i & 0 \\ 0 & n_y^i \\ n_y^i & n_x^i \end{bmatrix}, \quad \textit{and } \boldsymbol{H} = \begin{bmatrix} n_x & 0 \\ 0 & n_y \\ n_y & n_x \end{bmatrix}$$

$\boldsymbol{G}$ and $\boldsymbol{H}$ are the matrix representations of a crack element's out-normal and a crack face's normal directions, respectively. h_i is the element length.

The expressions for strain and stress are given by [23],

$$\boldsymbol{\varepsilon} = \boldsymbol{B}\boldsymbol{d} + (\boldsymbol{G} - \boldsymbol{\delta}_{\boldsymbol{T}^c} \boldsymbol{H}) [\![\boldsymbol{u}]\!] \tag{2.13}$$

$$\boldsymbol{\sigma} = \mathbb{C} : (\boldsymbol{B}\boldsymbol{d} + \boldsymbol{G}[\![\boldsymbol{u}]\!]) \tag{2.14}$$

where $\boldsymbol{B}$ is the standard matrix form of the shape function gradient, $\boldsymbol{d}$ is the nodal value of the coarse-scale displacement, and $\mathbb{C}$ is the elastic stiffness matrix. Substituting these expressions into the weak form Eqs. (2.4) and (2.6), the resulting coarse-scale and fine-scale equations are respectively given by

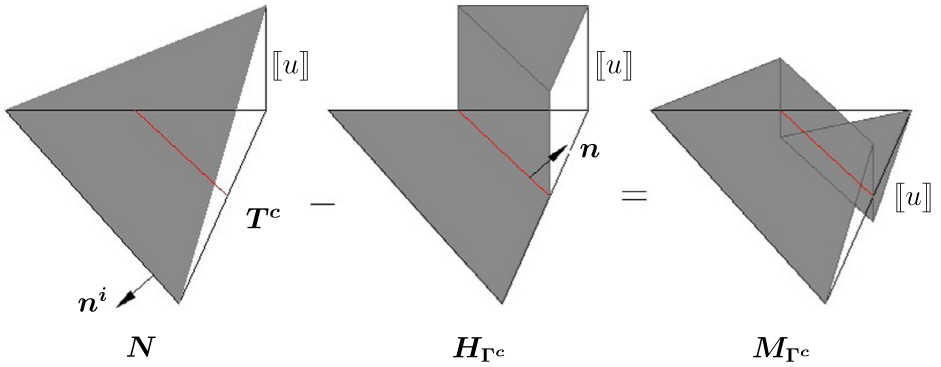

Fig. 3. Construction of discontinuous multiscale shape function in 2D. n^i is the element out-normal and n is the normal direction of the crack face.

$$\int_{\Omega} \boldsymbol{B}^T \mathbb{C} : (\boldsymbol{B}\boldsymbol{d} + \boldsymbol{G}[\![\boldsymbol{u}]\!]) dV = \int_{\Omega} \boldsymbol{N} f \, dV + \int_{\Gamma_h} \boldsymbol{N} T \, dS \tag{2.15}$$

$$\boldsymbol{H}^T \mathbb{C} : (\boldsymbol{B}\boldsymbol{d} + \boldsymbol{G}[\![\boldsymbol{u}]\!]) = \boldsymbol{T}^{\boldsymbol{c}} \tag{2.16}$$

The resulting system of equation is solved using an iterative procedure [23] resulting in a coarse-scale residual ($\bar{\boldsymbol{r}}$) and a fine-scale residual ($\boldsymbol{r}'$).

$$\bar{\boldsymbol{r}} = \int_{\Omega} \boldsymbol{B}^T \mathbb{C} : (\boldsymbol{B}\boldsymbol{d} + \boldsymbol{G}[\![\boldsymbol{u}]\!]) \, dV - \int_{\Omega} \boldsymbol{N} f \, dV - \int_{\Gamma_h} \boldsymbol{N} T \, dS \tag{2.17}$$

$$\boldsymbol{r}' = \boldsymbol{H}^T \mathbb{C} : (\boldsymbol{B}\boldsymbol{d} + \boldsymbol{G}[\![\boldsymbol{u}]\!]) - \boldsymbol{T}^{\boldsymbol{c}} \tag{2.18}$$

Linearization of the residual equations about $\boldsymbol{d}$ and $[\![\boldsymbol{u}]\!]$ gives the following system of equations in $\delta\boldsymbol{d}$, $\delta[\![\boldsymbol{u}]\!]$.

$$\begin{bmatrix} \boldsymbol{K}_{\bar{\boldsymbol{u}}\bar{\boldsymbol{u}}} & \boldsymbol{K}_{\bar{\boldsymbol{u}}\boldsymbol{u}'} \\ \boldsymbol{K}_{\boldsymbol{u}'\bar{\boldsymbol{u}}} & \boldsymbol{K}_{\boldsymbol{u}'\boldsymbol{u}'} \end{bmatrix} \begin{bmatrix} \delta\boldsymbol{d} \\ \delta[\![\boldsymbol{u}]\!] \end{bmatrix} = \begin{bmatrix} -\bar{\boldsymbol{r}} \\ -\boldsymbol{r}' \end{bmatrix} \tag{2.19}$$

where

$$\boldsymbol{K}_{\bar{\boldsymbol{u}}\bar{\boldsymbol{u}}} = \int_{\Omega} \boldsymbol{B}^{\boldsymbol{T}} \mathbb{C} \boldsymbol{B} \, dV \tag{2.20}$$

$$\boldsymbol{K}_{\bar{\boldsymbol{u}}\boldsymbol{u}'} = \int_{\Omega} \boldsymbol{B}^{\boldsymbol{T}} \mathbb{C} \boldsymbol{G} \, dV \tag{2.21}$$

$$\boldsymbol{K}_{\boldsymbol{u}'\bar{\boldsymbol{u}}} = \boldsymbol{H}^{\boldsymbol{T}} \mathbb{C} \boldsymbol{B} \tag{2.22}$$

$$\boldsymbol{K}_{\boldsymbol{u}'\boldsymbol{u}'} = \boldsymbol{H}^{\boldsymbol{T}} \mathbb{C} \boldsymbol{G} + \mathcal{H}_{\boldsymbol{n}} \boldsymbol{n} \otimes \boldsymbol{n} + \mathcal{H}_{\boldsymbol{m}} \boldsymbol{m} \otimes \boldsymbol{m} \tag{2.23}$$

The above finite element equations are solved using the static condensation method [23].

3. Cohesive model for fatigue

An important requirement for any phenomenologically based fatigue model is that it should be able to represent material degradation over time. The law we have used to represent this degradation is a modified form of the fatigue cohesive law developed by Maiti and Geubelle [22]. As shown in Fig. 4, for monotonic failure, the law is linear, whereas the law represents nonlinear behavior during cyclic loading. The main feature of this fatigue cohesive model is the difference between the loading and unloading paths in the traction–separation curve. This characteristic promotes sub-critical crack growth under cyclic loading due to progressive degradation of the cohesive properties, i.e. the slope of the traction–separation law.

The instantaneous Mode I cohesive stiffness $\mathcal{H}_n$ during reloading can be expressed as a nonlinear function of cohesive traction T_n^c and number of fatigue cycles as

$$\mathcal{H}_n = \frac{dT_n^c}{d[\![u_n]\!]} = f(T_n^c, N_f) \tag{3.1}$$

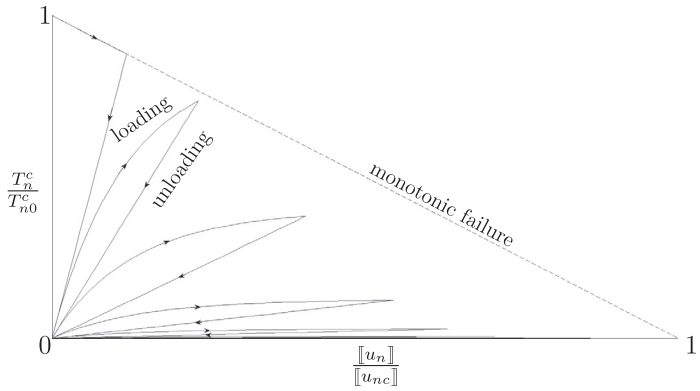

Fig. 4. Subcritical vs. critical failure. T_{n0}^c and $[\![u_{nc}]\!]$ are Mode I critical opening traction and displacement, respectively.

where N_f denotes the number of loading cycles experienced by a material point since the onset of failure, T_n^c denotes the normal component of traction on the crack face and $[\![u_n]\!]$ is the normal component of the displacement discontinuity on the crack face. A similar expression can be written for Mode II failure. A two-parameter power law relationship can be used to model the rate of decay of the cohesive stiffness $\mathcal{H}_n$.

$$\mathcal{H}_n = f(T_n^c, N_f) = -\gamma(N_f) T_n^c \tag{3.2}$$

where

$$\gamma = \frac{1}{\alpha} N_f^{-\beta} \tag{3.3}$$

Here α and β are cohesive parameters that are related to the degradation of the cohesive strength. The cohesive parameter α has the dimension of length while β denotes the history dependence of the failure process. Both of these parameters account for the unloading–reloading hysteresis. The inclusion of this hysteresis may, in the phenomenological sense, account for the dissipative mechanism arising from reverse yielding upon unloading. Reverse yielding upon unloading may occur when the crack growth happens as a result of alternating crystallographic slip [31]. This dissipative mechanism can also be caused as a result of repeated rubbing of asperities, which may cause steady weakening of the cohesive surfaces. A simple phenomenological model that incorporates this assumption has been built by relating the cohesive stiffness to the number of loading cycles through a power law relationship (3.2). The above evolution law can be expressed in terms of the rate of change of the cohesive stiffness $\mathcal{H}_n$ as

$$\dot{\mathcal{H}}_n = \begin{cases} -\frac{1}{\alpha} N_f^{-\beta} \mathcal{H}_n [\![\dot{u}_n]\!] & [\![\dot{u}_n]\!] \geqslant 0 \\ 0 & [\![\dot{u}_n]\!] < 0 \end{cases} \tag{3.4}$$

The second equation states that there is no change in cohesive stiffness during unloading cycle. Eq. (3.4) can be converted from the temporal to the spatial domain and, using a 1st order finite difference approximation, can be written as

$$\mathcal{H}_n^{(i+1)} = \mathcal{H}_n^{(i)} \left\{ 1 - \frac{1}{\alpha} N_f^{-\beta} \left([\![u_n]\!]^{(i+1)} - [\![u_n]\!]^{(i)} \right) \right\} \tag{3.5}$$

for $[\![\dot{u}_n]\!] \geqslant 0$, superscripts $(i+1)$ and (i) denote the adjacent load steps in a loading cycle. Thus, the traction–separation curve slope $(\mathcal{H}_n)$ is progressively degraded as the number of loading cycles increases.

There are four independent fatigue cohesive model parameters that have to be calibrated. Fracture strength (T_{n0}^c), area under the traction–separation curve, and critical displacement $([\![u_{nc}]\!])$ are three monotonic cohesive model parameters, of which only two are independent. For fatigue fracture, material parameters α and β are the additional two parameters that have to be calibrated. We can calibrate the first two monotonic cohesive model parameters by setting T_{n0}^c equal to the fracture strength of the elastic material and the area under the traction–separation curve equal to the Mode I fracture toughness G_I^c of the elastic material. The cohesive parameters α and β are calibrated from macro-scale experiments. The procedure for calibrating these two parameters is described in next section.

4. Results and discussions

In this section, examples are shown using this combined method (the VMM with the CZM) called the Variational Multiscale Cohesive Method (VMCM). These examples cover different concepts within fracture mechanics and are presented to show the capability of this method. Results are provided for the macroscopic stress intensity factor, the micro-structurally

short crack path, and fatigue crack growth. The later example is used to show that, by varying parameters α and β, fatigue crack growth curves of different materials can be predicted and inversely cohesive parameters α and β can also be calibrated from macro experiments. These examples demonstrate the capability of this method to model failure in materials at the macro-level as well as at the micro-level.

The objectivity of this method with respect to numerical discretization has already been demonstrated by Rudraraju et al. [23]. Unless otherwise noted, the material used is an epoxy [22] with $E = 3.9$ GPa, $\nu = 0.4$, and Mode I fracture toughness $G_{Ic} = 88.97\ \mathrm{J/m^2}$. The Mode I critical opening traction T^c_{n0} is taken to be 50 MPa, while the material parameters α and β are taken to be 5 μm and 0.5, respectively. In all numerical simulations, the length of the elements in front of the crack tip is defined to be smaller than $\frac{\pi}{8}\frac{E}{(1-\nu^2)}\frac{G_{Ic}}{\sigma_{avg}}$ [22] so that the fracture process is accurately captured in this region. Here, $\sigma_{avg}\ (T^c_{n0}/2)$ is the average stress in the cohesive zone. To concentrate more on the accuracy and benefits of this method, we present only the local Mode I simulation. Mode II and Mixed-Mode simulation can quite easily be carried out using this method. An in-house C++ based code has been developed to produce data for all the examples presented in this section. To solve the nonlinear equations that arise from the finite element formulations, a Newton–Raphson iterative scheme is used.

4.1. Comparison of the linear elastic stress intensity factor and the J-integral stress intensity factor

A comparison between the theoretical stress intensity factor and the numerical stress intensity factor is important to determine the accuracy of the stress field surrounding the crack using the VMM approach. This serves as a basic verification of the numerical method. The theoretical Mode I stress intensity factor (SIF) is calculated from a linear elastic fracture mechanics (LEFM) solution, while the numerical SIF is calculated using the *J*-integral method [32]. The SIF from linear elastic fracture mechanics is given by [33]

$$K_I = \sigma\sqrt{\pi a}\left\{1.12 - 0.23a/b + 10.6(a/b)^2 - 21.7(a/b)^3 + 30.4(a/b)^4\right\} \tag{4.1}$$

where σ is the applied stress, b is the height of the specimen and a is the crack length. The *J*-integral SIF is calculated along the contour Γ surrounding the boundary of a cohesive zone as shown in Fig. 5; this is given by Eq. (4.2).

$$J = \int_{\Gamma}\left(W\,dy - T_i\frac{\partial u_i}{\partial x}\,ds\right) \tag{4.2}$$

where W is the strain energy density, T_i is the ith component of the traction vector perpendicular to Γ in the outward direction, u_i is the ith component of the displacement vector, and ds is an arc length element along contour Γ. For plane strain conditions, the following relation is given by Rice [32]

$$K_I = \left[\frac{JE}{(1-\nu^2)}\right]^{1/2} \tag{4.3}$$

The LEFM requirement of small scale yielding imposes the condition that the cohesive zone size should be much less than the crack length ($\rho < a$) in order for the stress field outside the cohesive zone to be nearly the same as the *K*-dominant stress field. Thus, the cohesive zone size maintains a constant value of $\rho \approx 0.08$ mm, which is smaller than the initial crack length $a = 0.1$ mm.

The simulation parameters for calculating the *J*-integral from the FEM domain are the same as those used in the previous section.

As can be seen in Fig. 6, the numerically computed values for the SIF using the *J*-integral method are close to the SIF values predicted by LEFM. The small discrepancy between the two results can be attributed to the size of the cohesive zone, since the LEFM solution is valid only for small-scale yielding. Thus, using the VMCM, we can accurately capture the stress field surrounding the crack.

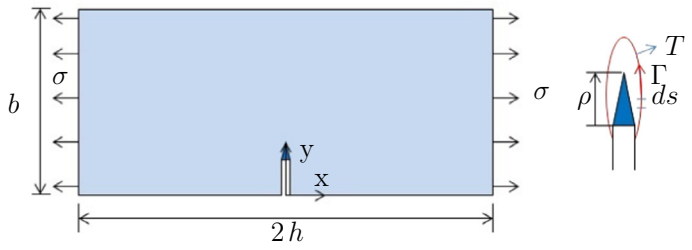

Fig. 5. *J*-integral path taken around the cohesive zone, $b = 1$ mm (cohesive zone length $\rho \approx 0.08$ mm).

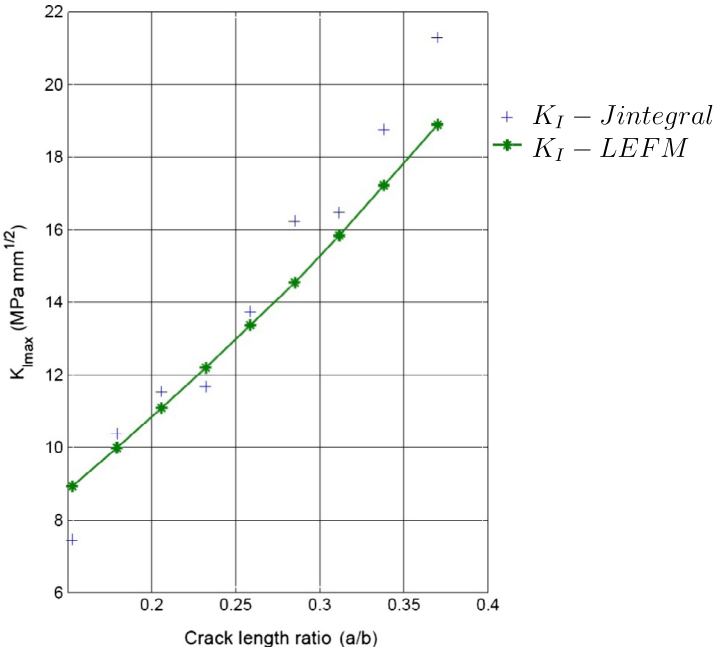

Fig. 6. Comparison between LEFM SIF and *J*-integral SIF.

4.2. Micro-structurally short surface crack propagation

The subject of micro-structurally short crack growth is used to show the ability of the VMCM to model two-dimensional micro-structural failure. Micro-structurally short crack growth refers to crack growth inside a grain (called trans-granular fracture) or at the grain boundaries (called inter-granular fracture). In this section, we show numerical simulation of crack growth across multiple grains where the crack could be a mixture of inter-granular and trans-granular fracture. In trans-granular fracture, the crack can follow either the slip planes or a plane lying in-between the slip planes.

The material model we use in our simulation is a hexagonal closed packed (HCP) Mg alloy, WE43, with five elastic constants and two lattice constants, as shown below,

$$C_{11} = 58 \text{ GPa}, \quad C_{12} = 25 \text{ GPa}, \quad C_{13} = 20.8 \text{ GPa},$$

$$C_{33} = 61.2 \text{ GPa}, \quad C_{55} = 16.6 \text{ GPa}.$$

$$c = 5.21 \text{ Å}, \quad a = 3.21 \text{ Å}$$

The material orientation data for individual grains are obtained from electron backscatter diffraction (EBSD) mapping (see Fig. 7), and the crack growth path image is obtained from scanning electron microscopy (SEM) of the WE43 surface [34]. Using the grain orientations (Euler–Bunge angles), elastic constants for individual grains are transformed from the crystal frame to the global simulation frame. These transformed 3-D elastic constants are converted to 2-D using plane stress assumptions. This way, the VMM is combined with 2-D crystal elasticity to model micro-structurally short crack growth. The mathematical formulations are similar to those described in Section 2, where the micro-structural domain contains the grain boundaries and $\mathbb{C}$ in Eq. (2.13) is the transformed 2-D elastic anisotropic stiffness matrix.

The HCP Mg has, in total, 18 slip systems, 3 basal $\langle a \rangle$, 3 prismatic $\langle a \rangle$, 6 pyramidal $\langle a \rangle$, and 6 pyramidal $\langle c + a \rangle$ slip systems. In pure Mg, the primary slip plane is the basal plane, but when Mg is alloyed with different materials, other slip planes become active. In the case of WE43, the crack growth mostly occurs along the basal and the pyramidal $\langle a \rangle$ planes [34]. To model a surface crack propagation problem using plane stress assumptions we use slip lines inside the grains. The slip lines are the intersections of the slip planes (basal and pyramidal $\langle a \rangle$) and the simulation plane. For our simulation, we use 1 basal slip line and 3 pyramidal $\langle a \rangle$ slip lines for simplicity. The crystal parameters for these 2 slip lines are taken from Choi et al. [35] and are shown below,

$$T_{crss}^{basal} = 25 \text{ MPa}, \quad T_{crss}^{pyramidal} = 68 \text{ MPa}$$

$$T_c^{gb} = 83 \text{ MPa}, \quad T_c^{gb\ cross} = 100 \text{ MPa}$$

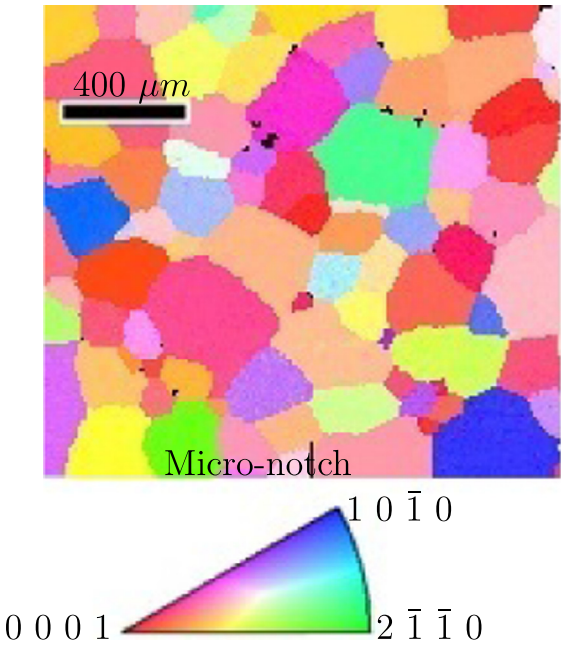

Fig. 7. EBSD image with orientation data of a Mg WE43 experimental specimen [34].

T_{crss} above corresponds to the critical resolved shear stress or the fracture strength of the slip plane, T_c^{gb} represents the grain boundary strength, and $T_c^{gb\ cross}$ is the increased grain boundary strength. The grain boundaries act as micro-structural barriers to short crack propagation, the strength of which varies with the crystallographic orientation relationship. The higher the tilt and twist mis-orientation angles between adjacent slip bands the more effective the grain boundaries are as barriers to the transmission of slip into the adjacent grains. This also holds true for the crack growth from one grain to another grain across a grain boundary, and this increased grain boundary strength is labeled here as $T_c^{gb\ cross}$. A constant value of $T_c^{gb\ cross}$ is used to concentrate more on the varied applications of the VMCM. The crack growth along the slip lines is characterized as Mode II fracture, while the crack growth along the grain boundary is Mode I fracture.

In this simulation, there are six cohesive traction–separation laws to account for 1 basal slip crack (Mode II), 3 pyramidal slips crack (Mode II), 1 grain boundary cracking (Mode I), and 1 grain boundary crossing. For all these laws, we use a critical sliding/opening displacement value of 0.1 μm.

For a tension test, in a elastic material, the crack on the macroscopic level will grow perpendicular to the direction of the maximum principal stress. However, at the microscopic level, the cracks can only grow along certain planes within a grain. These planes are the slip planes, and for a Mg WE43 alloy, the crack grows predominantly along the basal plane and the pyramidal plane [34]. Thus, to model this crack path, we developed a crack tracking algorithm that takes into account all of these paths. At the crack tip, the algorithm searches through all the favorable lines (i.e. 1 basal and 3 pyramidal planes within a grain or 1 basal, 3 pyramidal, and 1 grain boundary at the grain boundary) that meet the fracture criteria and selects the line whose normal is closest to the maximum principal stress direction. This way, the crack grows along the slip lines and/or along the grain boundaries.

The finite element mesh for this model is created using a real micro-structural image. The model domain consists of 82 grains with different orientations as shown in the color[1] plot (Fig. 7). The grain edges of this real micro-structure are generated using ImageJ [36], and then the OOF [37] program is used to generate a finite element mesh from these edges. The steps outlined above are shown in Fig. 8. The size of the micro-notch in Fig. 8(c) is similar to the size of experimental micro-notch.

The boundary conditions for this simulation are applied so as to match the experimental boundary conditions. In the experiment, the specimen is loaded in tension along the RD direction [34]. To produce similar loads on our model boundaries, we apply tensile loads on the left and right boundaries of Fig. 8(c), while loads from Poisson's effect ($\nu = 0.27$) are applied on the top and bottom boundaries. The loading is applied until the micro-structural crack reaches the domain boundary.

In Fig. 9, we show the comparison between the experimental crack path and our numerical crack path. Fig. 9(b) is a superposition of the EBSD image with the numerical crack path. This figure also contains basal slip lines to show that the crack

[1] For interpretation of color in 'Fig. 7', the reader is referred to the web version of this article.

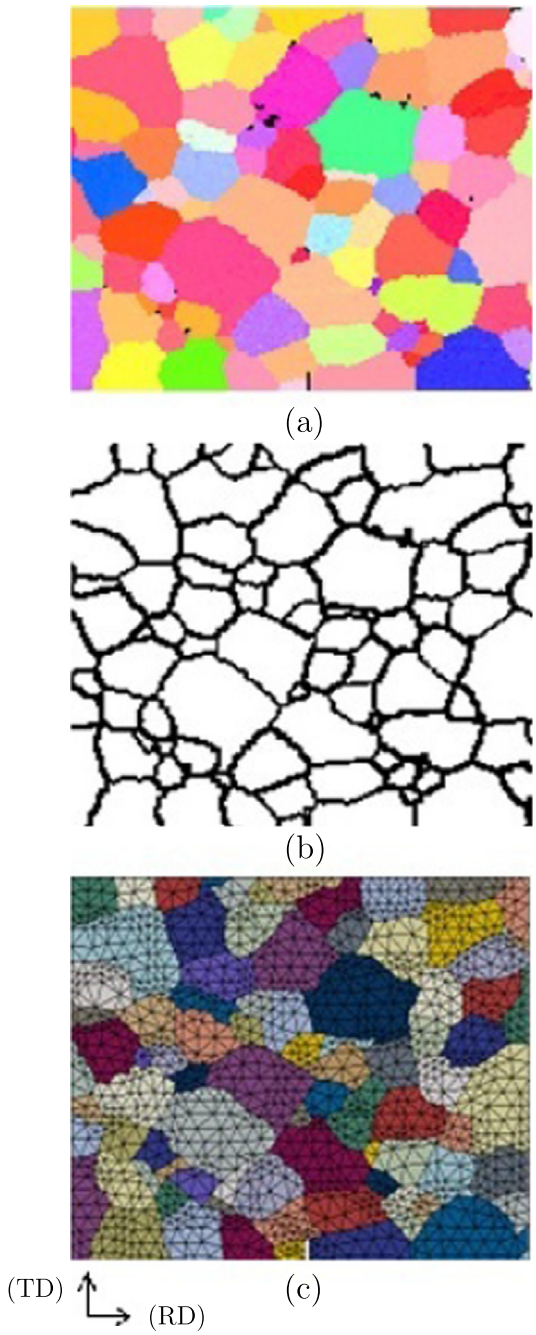

Fig. 8. FE mesh generated from a real micro-structure image, RD – Rolled direction, TD – Transverse direction. (a) EBSD image [34]. (b) Grains edges generated from ImageJ [36]. (c) FE mesh generated from OOF [37] with colors shown only for distinguishing different grains. (For interpretation of the references to color in this figure legend, the reader is referred to the web version of this article.)

growth inside a grain closely follows these slip lines. On comparing these two figures (Fig. 9(a) and (b)), we see that the crack path predicted using the VMCM method is close to the experimental crack path even when using a coarse mesh. The differences between these two crack paths are due to our assumptions of constant grain boundary strength $\left(T_c^{gb}\right)$ and plane stress and due to the use of a constant $T_c^{gb\ cross}$ value for all grain boundaries. These parameters need to be more carefully calibrated for the alloy from lower-scale simulations and/or experiments so that the crack path can be better reproduced. The short fatigue crack growth can also be modeled using the VMCM. However, for each cohesive law, there are two additional parameters α and β that have to be calibrated, along with the above-mentioned parameters. The fatigue parameters α and β are

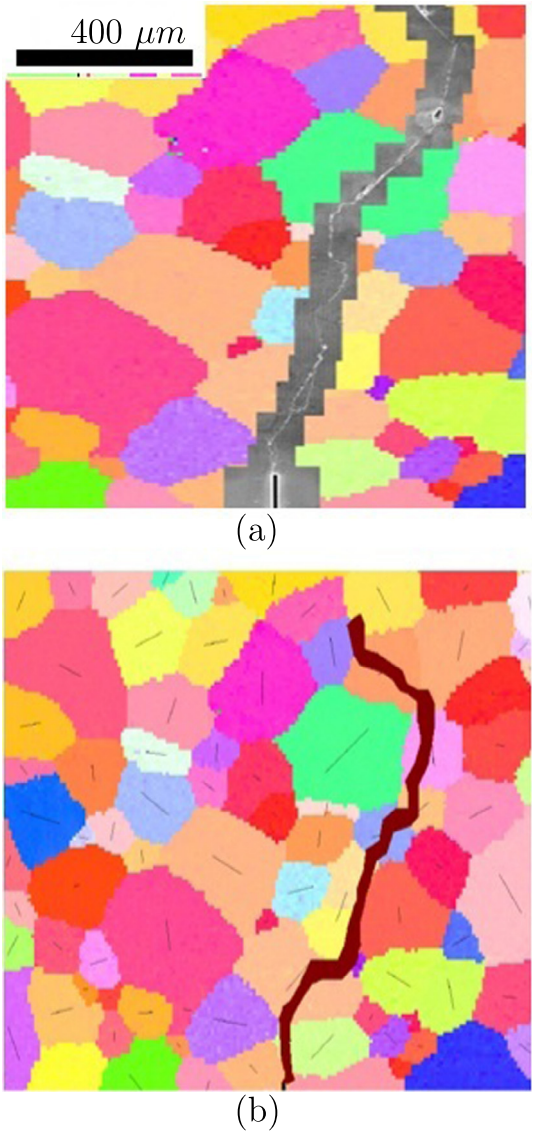

Fig. 9. Comparison of experimental crack path and numerical crack path. (a) Experimental crack image – SEM crack image superimposed on EBSD image [34]. (b) VMCM crack path (shown in dark red) superimposed on EBSD image with basal slip lines shown in each grain. (For interpretation of the references to color in this figure legend, the reader is referred to the web version of this article.)

linked to each slip system. Thus, experimental fatigue crack growth rates for each individual slip system are needed to calibrate these two parameters. The crack growth rates for each slip system can be measured through method, such as benchmarking [38] or striations.

4.3. 'Local' Mode I fatigue crack growth

For fatigue crack growth, we have again considered the SENT specimen (Fig. 5). The crack evolution is considered to be 'local' Mode I, which implies that, in the direction of crack path, there is no shear stress, and the Mode II fracture toughness is zero. In Fig. 5, the left boundary of the specimen has no displacement in the x-direction, and the bottom left corner of the specimen has zero displacement in the y-direction. Fatigue tests of specimens are carried out under displacement-controlled tension loading (Fig. 10). The shape of the applied displacement does not affect the fatigue behavior, as the rate dependence of the material is ignored. The maximum displacement Δ_{max} is taken to be $0.009b$, the initial crack length is $a_0 = 0.1b$, and the amplitude ratio $R\left(\frac{\sigma_{max}}{\sigma_{min}}\right)$ *is 0.*

Fig. 11 shows the evolution of traction–separation for a point on the cohesive zone. In the finite element model, this is the third element in the crack path. We can clearly see the dissipation between the loading–unloading cycles in this element. The

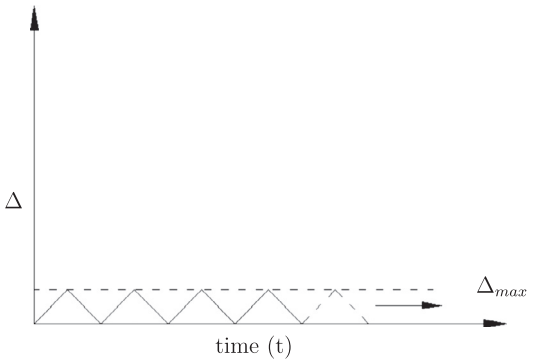

Fig. 10. Variation of applied displacement Δ with time.

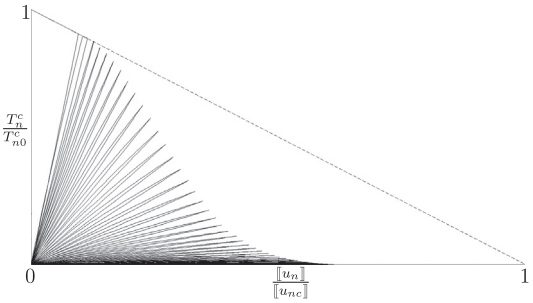

Fig. 11. Evolution of traction–separation curve for a point on the cohesive zone.

dotted line in this figure is the monotonic failure line and is shown to indicate the sub-critical nature of the fatigue cracks. The nonlinear nature of the maximum crack opening traction per cycle can also be clearly seen in this figure.

Fig. 12 shows σ_{xx} distribution snapshots taken at different cycles. The crack has propagated ≈ 0.3 times the total width of the specimen after 2200 cycles. After this cycle,

$$K_I = 22 \text{ MPa } \sqrt{\text{mm}} \ (\approx K_{Ic} = 22.21 \text{ MPa } \sqrt{\text{mm}}) \tag{4.4}$$

and the crack propagates rapidly, indicating the final failure (K_{Ic} is monotonic fracture toughness) is as predicted by the LEFM solution.

As can be inferred from the above statement, the curve of the crack path versus the number of loading cycles (Fig. 13) should be asymptotic. This is the expected behavior of the fatigue crack growth in the case of a SENT specimen. To get the Paris curve, we need the applied stress intensity factor. The applied stress intensity factor (K_I) is calculated using the *J*-integral method [32]. The details of K_I calculation are given in Section 4.1. By differentiating the crack length with respect to the number of loading cycles (Fig. 13), we can calculate the crack growth rate (da/dN) and plot it versus the change in stress intensity factor (ΔK_I). This curve represents the steady state crack growth rate (Fig. 14). The curve captures the final failure quite well as indicated by Eq. (4.4). The slope of this curve (Fig. 14) is m = 2.5 and the intercept $C \approx 10^{-07}$ mm/cycle.

4.4. Effect of parameters α and β on the Paris curve

In this section, we do a parametric study on the effect of cohesive parameters α and β on the crack growth rate and the Paris curve. Fig. 15 plots crack tip advancement versus the number of loading cycles for three different values of α, while $\beta = 0.2$ is kept constant. As can be seen in this figure, the crack growth rate decreases as α increases. For $\alpha = 2$ μm, the crack advances nearly 0.4 times the width of the specimen in 80 cycles, whereas, for $\alpha = 5$ μm, the crack takes around 240 cycles to advance the same distance. Differentiating the crack length with respect to the number of cycles, we can plot (Fig. 16) the crack growth rate (da/dN) versus the change in stress intensity factor (ΔK_I). Thus, for different values of α, we get Paris curves with different intercepts ($C = 1 \times 10^{-06}$ to 3×10^{-06} mm/cycle). Thus, for the same stress intensity factor we can get different crack growth rates and by changing α we can change these rates.

In Fig. 17, the plot of crack length versus number of cycles for different β-values is shown. For different values of β (0.1, 0.3, and 0.5), the crack growth rate changes, and by differentiating these curves we get different Paris curves (Fig. 18) with

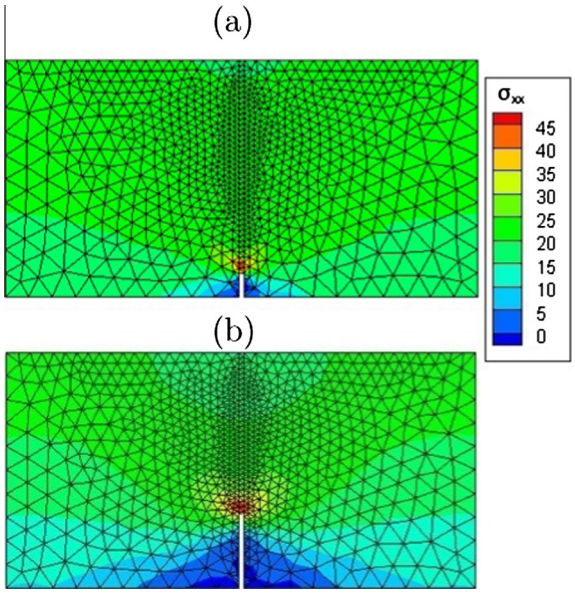

Fig. 12. σ_{xx} stress (MPa) distribution for 'local' Mode I fatigue crack growth. (a) Stress distribution at the end of the first cycle. (b) Stress distribution at the end of 2200 cycles (cracked elements have been removed from the plot).

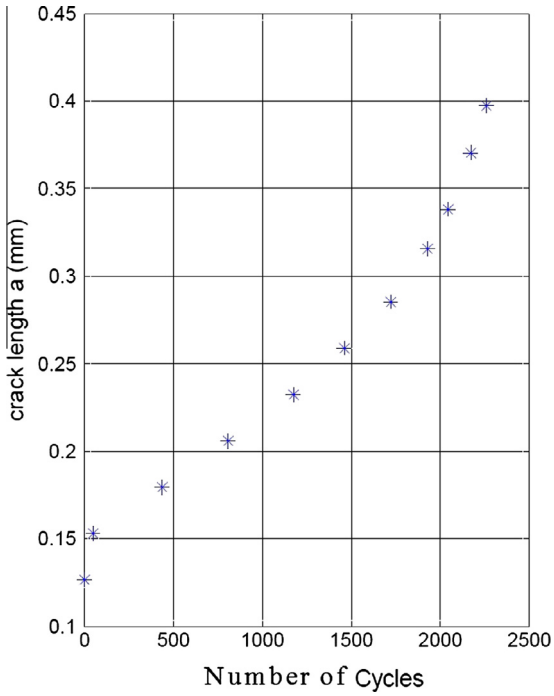

Fig. 13. Fatigue crack growth in SENT specimen versus the number of loading cycles.

different slopes ($m = 2.5$ to $3.3, C \approx 10^{-07}$ mm/cycle). Thus, by changing these two parameters, one can obtain Paris curves for different materials.

This procedure is followed with polystyrene [39], which has $E = 3.1$ GPa, $\nu = 0.35$, and Mode I fracture toughness $G_{Ic} = 1164.52$ J/m^2. The Mode I critical opening traction T^c_{n0} is taken to be equal to the craze stress, 38 MPa [39]. The parameters α and β are calibrated from the experimental data [40], and the parameters are found to be in the range of

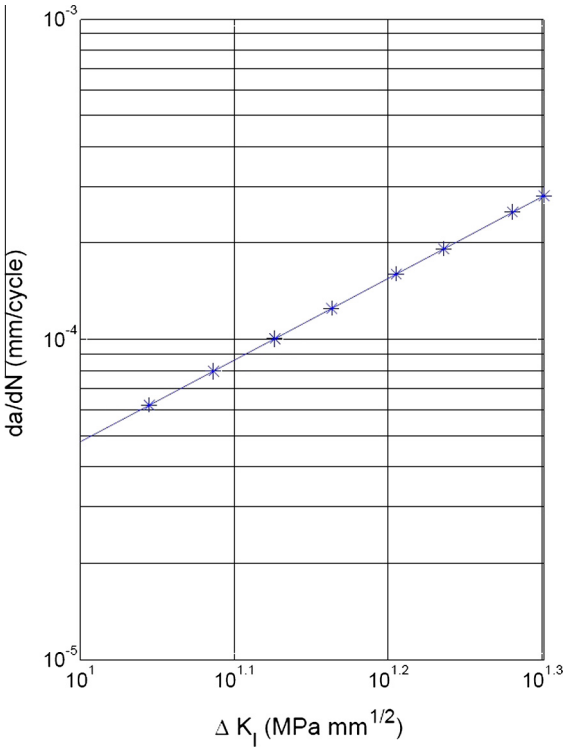

Fig. 14. Paris curve, $\alpha = 5$ μm and $\beta = 0.5$.

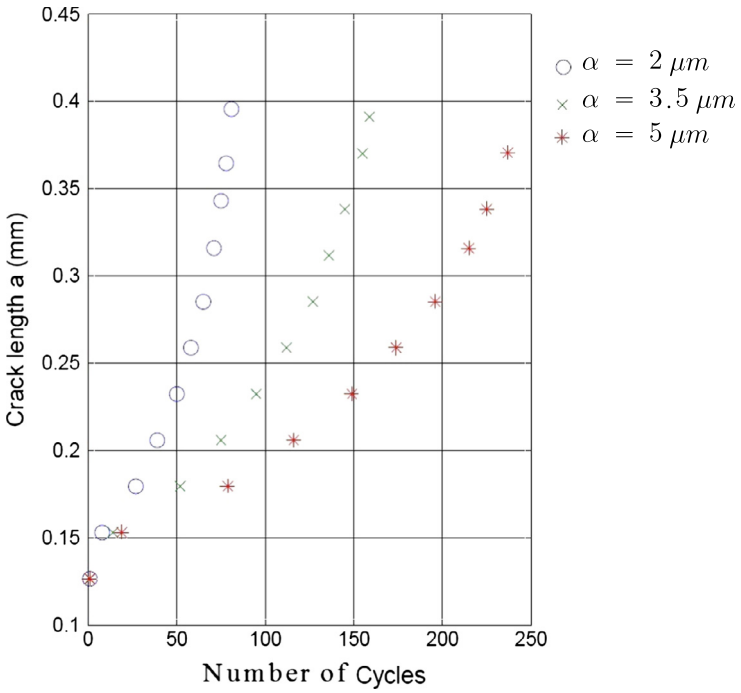

Fig. 15. Effect of α parameter on crack propagation ($\beta = 0.2$).

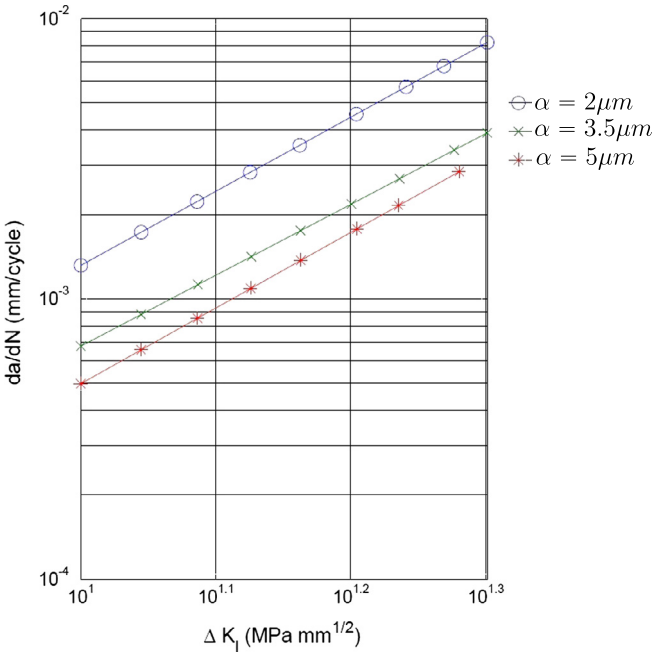

Fig. 16. Paris curves for different values of α ($\beta = 0.2$).

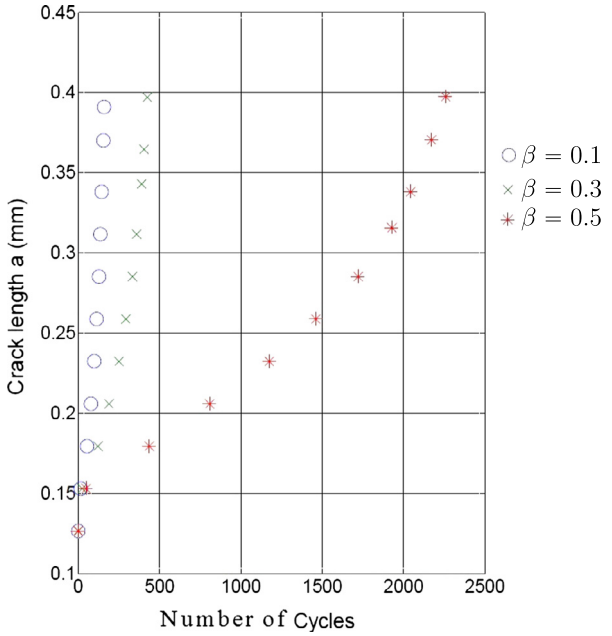

Fig. 17. Effect of β parameter on crack propagation ($\alpha = 5$ μm).

0.03–0.05 mm and 0.5, respectively (Fig. 19). The simulations were run on 150 mm × 50 mm × 3 mm SENT specimens with an initial crack length of $a_0 = 20$ mm [39].

Future work will involve microscopic interpretation of α and β using localized grain-to grain crack growth rate measurements.

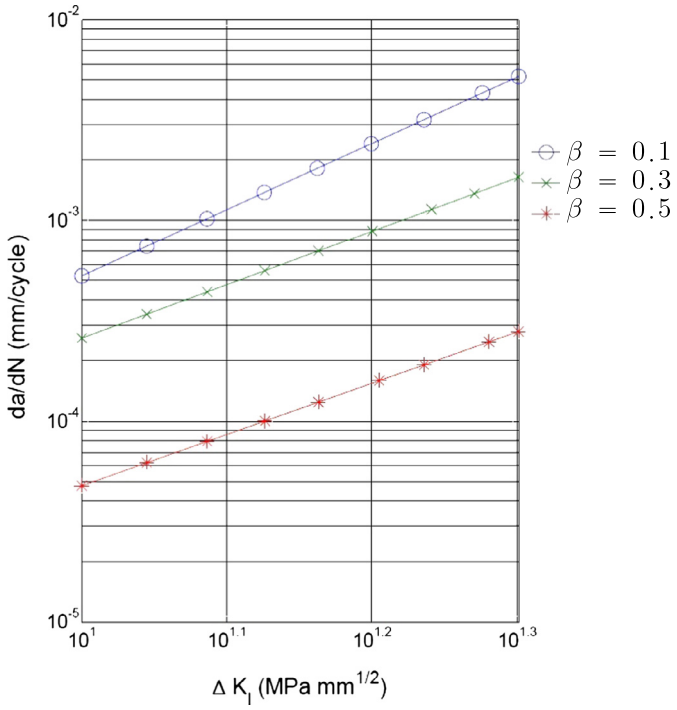

Fig. 18. Paris curves for different values of β (α = 5 μm).

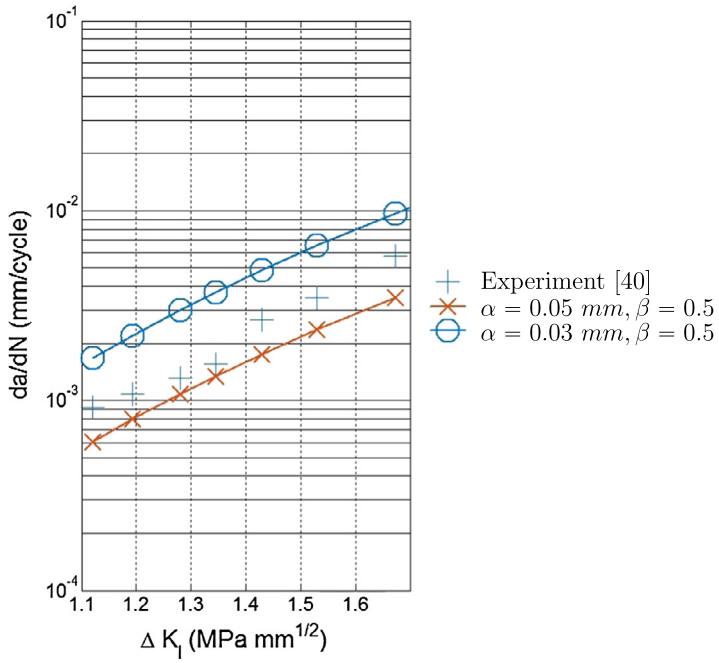

Fig. 19. α and β parameters calibrated for polystyrene [39].

5. Conclusion

Modeling fatigue failure is valuable for predictive modeling of component life and ensuring structural integrity in aerospace structures. In this paper, the variational multiscale method (VMM) is used to model fatigue crack propagation for the first time. In this approach, a discontinuous displacement field is added to elements that exceed the critical values of normal

or tangential traction during loading. This additional degree of freedom is represented within the cracked element using a special discontinuous shape function, which ensures that the displacement jump is localized to that particular element. The finite element formulation and code implementation details are presented. Compared to traditional cohesive zone modeling approaches, this method does not require the use of any special interface elements in the micro-structure. This method is shown to produce accurate stress field near the crack tip. A micro-structurally short crack growth simulation is performed along with an experimental comparison to demonstrate the accuracy of this method in predicting microscopic crack paths and Mixed-Mode failure. A two-parameter phenomenological fatigue cohesive law is incorporated into the VMM via a traction continuity equation. The relationship between the phenomenological model parameters and the slope and intercept of the Paris curve are shown. We have shown that different Paris curves can be simulated by varying the parameters in the cohesive law. As an example, we have performed a comparison between our fatigue model and published experimental data. Future work will focus on developing a micro-mechanical interpretation of these parameters and their calibration with experimental data.

Acknowledgments

The authors would like to acknowledge Professor John Allison, Professor J. Wayne Jones, and their graduate student Jacob Adams, of Material Science Engineering Department at the University of Michigan, Ann Arbor for providing the experimental data. The computations have been carried out as part of research supported by the U.S. Department of Energy, Office of Basic Energy Sciences, Division of Materials Sciences and Engineering under Award No. DE-SC0008637 that funds the PRedictive Integrated Structural Materials Science (PRISMS) Center at the University of Michigan.

References

[1] Armero F, Garikipati K. An analysis of strong discontinuities in multiplicative finite strain plasticity and their relation with the numerical simulation of strain localization in solids. Int J Solids Struct 1996;33(20–22):2863–85.
[2] Bažant Z. Mechanics of distributed cracking. Appl Mech Rev 1986;39:675–705.
[3] Larsson R, Runesson K, Ottosen NS. Discontinuous displacement approximation for capturing plastic localization. Int J Numer Methods Eng 1993;36:2087–105.
[4] Ramakrishnan N, Okada H, Atluri SN. On shear band formation: II. Simulation using finite element method. Int J Plasticity 1994;10(5):521–34.
[5] Oliver J, Huespe AE, Sanchez PJ. A comparative study on finite elements for capturing strong discontinuities: E-FEM vs X-FEM. Comput Methods Appl Mech Eng 2006;195:4732–52.
[6] Hughes TJR. Multiscale phenomena: Greens functions, the Dirichlet-to Neumann formulation, subgrid scale models, bubbles and the origins of stabilized methods. Comput Methods Appl Mech Eng 1995;127:387–401.
[7] Garikipati K. A variational multiscale method to embed micromechanical surface laws in the macromechanical continuum formulation. Comput Model Eng Sci 2002;3:175–84.
[8] Griffith AA. The phenomena of rupture and flow in solids. Philos Trans Roy Soc Lond A 1921;221:163–98.
[9] Irwin G. Analysis of stresses and strains near the end of a crack traversing a plate. J Appl Mech 1957;24:361–4.
[10] Dugdale DS. Yielding of steel sheets containing slits. Int J Mech Phys Solids 1960;8(2):100–4.
[11] Barenblatt G. The mathematical theory of equilibrium cracks in brittle fracture. Adv Appl Mech 1962;7:55–129.
[12] Willis JR. A comparison of the fracture criteria of Griffith and Barenblatt. J Mech Phys Solids 1967;15(3):151–62.
[13] Hillerborg A, Modeer M, Petersson PE. Analysis of crack formation and crack growth in concrete by means of fracture mechanics and finite elements. Cem Concr Res 1976;6(6):773–81.
[14] Bažant ZP, Oh B. Crack band theory for fracture of concrete. Mater Struct 1983;16:155–77.
[15] Rots J, Nauta P, Kuster G, Blaauwendraad J. Smeared crack approach and fracture localization in concrete, vol. 30. Delft: Delft University of Technology; 1985.
[16] Xu XP, Needleman A. Numerical simulations of fast crack-growth in brittle solids. J Mech Phys Solids 1994;42(9):1397–434.
[17] Camacho GT, Ortiz M. Computational modeling of impact damage in brittle materials. Int J Solids Struct 1996;33(20–22):2899–938.
[18] de Andres A, Perez J, Ortiz M. Elastoplastic finite element analysis of three-dimensional fatigue crack growth in aluminum shafts subjected to axial loading. Int J Solids Struct 1999;36:2175–320.
[19] Nguyen O, Repetto E, Ortiz M, Radovitzky R. A cohesive model for fatigue crack growth. Int J Fract 2001;110:351–69.
[20] Roe K, Siegmund T. An irreversible cohesive zone model for interface fatigue crack growth simulation. Eng Fract Mech 2003;70:209–32.
[21] Yang B, Mall S, Ravi-Chandar K. A cohesive model for fatigue crack growth in quasibrittle materials. Int J Solids Struct 2001;38:3927–44.
[22] Maiti S, Geubelle PH. A cohesive model for fatigue failure of polymers. Eng Fract Mech 2005;72:691–708.
[23] Rudraraju S, Salvi A, Garikipati K, Waas AM. Predictions of crack propagation using a variational multiscale approach and its application to fracture in laminated fiber reinforced composites. Compos Struct 2012;94:3336–46.
[24] Rocco C, Guinea GV, Planas J, Elices M. Review of the splitting-test standards from a fracture mechanics point of view. Cem Concr Res 2001;31:73–82.
[25] Yamakov V, Saether, Phillips D, Glaessgen E. Molecular-dynamics simulation-based cohesive zone representation of inter-granular fracture processes in aluminum. J Mech Phys Solids 2006;54:1899–928.
[26] He M, Li S. An embedded atom hyperelastic constitutive model and multiscale cohesive finite element method. Comput Mech 2012;49(3):337–55.
[27] Temam R, Strang G. Functions of bounded deformation. Arch Ration Mech Anal 1980;75:7–21.
[28] Simo JC, Oliver J, Armero F. An analysis of strong discontinuities induced by strain-softening in rate-independent inelastic solids. Comput Mech 1993;12:277–96.
[29] Simo JC, Oliver J. A new approach to the analysis and simulation of strain softening in solids 1994:25–39.
[30] Sundararaghavan V, Sun S. Modeling crack propagation in polycrystalline alloys using a variational multiscale cohesive method. 2nd World congress on integrated computational materials and engineering, vol. 36. Hoboken (NJ, USA): John Wiley and Sons, Inc; 2013.
[31] Kanninen M, Popelar C. Advanced fracture mechanics. Oxford: Oxford University Press; 1985.
[32] Rice JR. A path independent integral and the approximate analysis of strain concentration by notches and cracks. J Appl Mech 1968;35:379.
[33] Perez N. Fracture mechanics. Kluwer Academic Publisher; 2004.
[34] Allison J, Jones JW. Personal communication. Ann Arbor: Material Science and Engineering Department at University of Michigan; 2015.
[35] Choi S-H, Kim D, Park S, You B. Simulation of stress concentration in mg alloys using the crystal plasticity finite element method. Acta Mater 2010;58(1):320–9.
[36] National Institute of Health. ImageJ: image processing and analysis in Java. <http://imagej.nih.gov/ij/index.html>.

[37] National Institute of Standards and Technology (U.S. Department of Commerce). OOF: finite element analysis of microstructures. <http://www.ctcms.nist.gov/oof/>.
[38] McBagonluri F, Akpan E, Mercer C, Shen W, Soboyejo W. An investigation of the effects of microstructure on dwell fatigue crack growth in Ti-6242. Mater Sci Eng: A 2005;405(1):111–34.
[39] Marshall G, Culver L, Williams J. Fracture phenomena in polystyrene. Int J Fract 1973;9(3):295–309.
[40] Skibo M, Hertzberg R, Manson J. Fatigue fracture processes in polystyrene. J Mater Sci 1976;11(3):479–90.